Materials Today Advances 20 (2023) 100439

Contents lists available at ScienceDirect

Materials Today Advances

journal homepage: www.journals.elsevier.com/materials-today-advances/

Dynamic mechanical performance of FeNiCoAl-based high-entropy alloy: Enhancement via microbands and martensitic transformation

Aomin Huang [a], Cheng Zhang [b,c,d,**], Zezhou Li [a], Haoren Wang [e], Mingjie Xu [f], Chaoyi Zhu [a], Xin Wang [g], Marc A. Meyers [a,e], Enrique J. Lavernia [b,*]

[a] Materials Science and Engineering Program, University of California San Diego, La Jolla, CA, 92093-0418, USA
[b] Department of Materials Science and Engineering and Department of Mechanical Engineering, Texas A&M University, College Station, TX, 77840, USA
[c] Tianmushan Laboratory, Hangzhou, 310023, People's Republic of China
[d] Center for Alloy Innovation and Design, State Key Laboratory for Mechanical Behavior of Materials, Xi'an Jiaotong University, Xi'an, 710049, People's Republic of China
[e] Department of NanoEngineering, University of California San Diego, La Jolla, CA, 92093-0448, USA
[f] Department of Materials Science and Engineering, University of California Irvine, Irvine, CA, 92697-2585, USA
[g] Department of Metallurgical and Materials Engineering, the University of Alabama, Tuscaloosa, AL, 77840, USA

ARTICLE INFO

Keywords:
High-entropy alloy
Deformation-induced microband
Martensitic transformation
Dynamic deformation

ABSTRACT

The non-equiatomic FeNiCoAlTaB high-entropy alloy exhibits outstanding quasi-static mechanical properties. Here, we investigate the microstructural evolution and mechanical response of this alloy subjected to dynamic loading, which has not been done before. A novel strategy combining extensive microbanding and martensitic transformation improves the resistance to the plastic instability by deterring the formation of adiabatic shear bands, that only occur beyond a critical shear strain larger than 4. The aged alloy, with grain sizes up to 400 μm, exhibits a dynamic yield stress over 1300 MPa with good deformability in this regime. This investigation sheds light on potential strategies for the enhancement of dynamic mechanical properties of structural materials through the use of a stress-induced martensitic transformation.

1. Introduction

As a new class of metallic materials, high-entropy alloys (HEAs) consisting of five or more elements are changing the strategy of alloy design [1,2]. The concept of non-equiatomic HEAs or multi-principal element alloys (MPEAs) further expands their compositional space [3]. Recent studies in this area have shown that HEAs can indeed attain exceptional mechanical properties in a broad range of temperatures. For example, outstanding fracture toughness and damage resistance under cryogenic conditions [4,5], a combination of high strength and ductility at ambient temperature [6–11], and ultrahigh strength at high temperatures [12,13] have been achieved for HEAs. These superb mechanical properties render HEAs promising candidates for critical structural applications [14].

However, review of the published literature shows that most of reported mechanical properties of HEAs are measured under quasi-static conditions and, as a consequence, studies in the high strain rate regime are quite limited. Two exceptions to this are the well-known Cantor alloy (CoCrFeMnNi) and Al-doped FeNiCoCr HEAs [15–20]. The design and fabrication of HEAs with high strength and deformability under high strain rate conditions can help to expand the potential range of critical applications, such as impact-resistant structures [21–23]. It is important to emphasize that when metallic materials are exposed to high external loading rates, distinctive deformation behaviors can arise. This is primarily caused by insufficient time for heat dissipation, elevated dislocation velocities, and the activation of alternative deformation mechanisms. The inadequate heat dissipation will eventually lead to a predominantly adiabatic deformation, rather than an isothermal one, resulting in a temperature increase [24]. Such phenomenon is often followed by shear localization, which is also observed in various metallic materials, such as tantalum [25], Al–Li alloys [26], Al alloys [27], copper [28] and Ti–6Al–4V alloy [29]. This shear

* Corresponding author.
** Corresponding author. Department of Materials Science and Engineering and Department of Mechanical Engineering, Texas A&M University, College Station, TX, 77840, USA.
E-mail addresses: chz040@eng.ucsd.edu (C. Zhang), lavernia@tamu.edu (E.J. Lavernia).

https://doi.org/10.1016/j.mtadv.2023.100439
Received 12 July 2023; Received in revised form 27 October 2023; Accepted 5 November 2023
Available online 17 November 2023

localization is associated with rotational dynamic recrystallization and eventually causes catastrophic failure. Therefore, deterring its onset is essential for structural materials.

The martensitic transformation induced by deformation can be typically classified into stress-induced and strain-induced, depending on the required activation free energy. Formation of strain-induced martensite relies heavily on accumulated plastic strain, which in turn makes them more preferential at heavily defected areas, like shear-band and twin intersections [30]. Stress-induced martensite, on the other hand, shares the same nucleation sites with the spontaneous thermally induced martensitic transformation [31]. The strain-induced martensitic transformation is generally activated in a stabilized austenite matrix after the onset of dislocation slip [32]. Such mechanisms have been extensively studied in metastable alloys, for instance, TRIP steels [33–36]. In addition to conventional TRIP steels, stress-induced martensitic transformation, which is primarily related to stress state [37], has also been induced in dual-phase metastable HEAs [38,39], Ti-rich TiZrHfAlNb HEA [40], and refractory $TiZrHfTa_x$ HEAs [41], to enhance their mechanical properties. For example, Tanaka et al. [42] reported an excellent superelastic effect (above 13 %) achieved via FCC-γ to BCT/BCC-α' martensitic transformation in an Fe–Ni–Co–Al–Ta–B alloy. Zhang et al. [9] also reported a stress-induced martensitic transformation coupled with the formation of deformation-induced microbands. They obtained a high yield strength ~1.2 GPa and ultimate tensile strength ~1.7 GPa.

In the regime of high strain-rate deformation, thermal softening becomes more prevalent, which significantly weakens strain hardening. The steady formation of stress-induced martensite demands sustained strain hardening and reasonable deformability. Given the strain hardening effect provided by microbanding, steady formation of martensite occurs. Thus, introducing microbands helps to maintain reasonable strain hardening rate, which in turn gives rise to the steady formation of martensite. In addition, due to the high solvus temperature of NiAl grain boundary precipitates, fine grains are difficult to form without sacrificing ductility. Therefore, grain refinement must be avoided to obtain clean grain boundaries without NiAl precipitates [43]. Here, we report on a feasible and novel strategy to improve the dynamic mechanical properties of a coarse-grained Fe-27.5Ni-17.5Co-10.5Al-2.2Ta-0.05B HEA by introducing microbands as a means to enhance the formation of martensite. More specific goals of this study include: (1) the characterization of the microstructure evolution under varying loading conditions; (2) the establishment of the deformation mechanisms at high rates. (3) the study of the martensitic transformation during dynamic testing.

2. Experimental methods

2.1. Materials preparation and mechanical tests

The Fe–Ni–Co–Al–Ta–B ingots were fabricated through arc-melting followed by hot rolling at 1250 °C with a reduction in thickness of ~30 %. Thereafter, the aging treatment proceeded at 600 °C for 24 h. Cylindrical specimens with dimensions of 3.6 mm × 3.6 mm and 3.6 mm × 5.4 mm (diameter × height) were prepared by electrical discharge machining for dynamic and quasi-static compression testing, respectively. The height/diameter ratio was adjusted to ensure homogeneous deformation during compressive testing and reduce the inertia effect, buckling and frictional force. The height/diameter ratio of 1.0 and 1.5 are standardized dimensions for uniaxial dynamic and quasi-static compression tests, respectively [44–47]. In addition, hat-shaped specimens were machined to impose localized strain, forcing shear band formation in a narrow region. The dimensions of hat-shaped specimens and determination of shear stress/strain are shown in Fig. S1.

The compressive properties and shear deformation of Fe–Ni–Co–Al–Ta–B were acquired at various levels of strain rate ranging from 10^{-3} to 10^{5} s^{-1}. Cylindrical specimens were tested statically via Instron uniaxial testing machine (Model 3367) and dynamically via split Hopkinson pressure bar (SHPB) [48]. The strain rates of quasi-static compression tests were 10^{-3} s^{-1}, 10^{-2} s^{-1} and of dynamic test compression was ~10^{3} s^{-1}. In addition, the shear strain rate in the dynamic shearing test was as high as 10^{5} s^{-1}. By placing a stopper ring between the incident bar and transmitted bar, the strain in dynamic impact tests was controlled. Three samples were tested in each condition, including dynamic and quasi-static. The calculation of engineering and true stress, engineering and true strain and strain rates was carried out through standard equations provided in Supplementary Materials.

2.2. Microstructure characterization

Well-ground and polished specimens were used to characterize the deformation mechanisms and corresponding microstructures. X-ray diffractometry (XRD, Rigaku, Smartlab) was initially applied to confirm the crystalline structure of the alloy. The time per step (step size is 0.02°) was 1s, with a scanning angle from 30° to 100° by using Cu-Kα (λ = 0.154 nm). The microstructure and grain orientation characterization were performed on a field-emission scanning electron microscope (SEM, FEI Apreo) equipped with energy dispersive spectrometer (EDS, Oxford instruments) and electron backscattered diffraction detector (EBSD, Oxford instruments). Initial phase determination at various strain levels was established by EBSD, followed by further identification performed by transmission electron microscopy (TEM). Specimens of selected areas for TEM observation were prepared by focused Ga^{+} source ion beam milling through FIB-SEM (FEI Scios Dual Beam focus ion beam SEM). The microstructures generated by plastic deformation were initially characterized via EBSD and SEM. Related geometrically necessary dislocation (GND) densities were calculated by an in-house program [49,50]. Further studies of the martensite phases and heterogeneous substructures were conducted via S/TEM (Scanning transmission electron microscopy, JEOL, Grand Arm) performed at 300 KV and TEM (JEOL, 2800) operated at 200 KV. Additional identification and characterization of microstructure within shear bands in dynamically sheared hat-shaped specimens was carried out via EBSD and TEM. Precession electron diffraction (PED) [51] was operated in a STEM mode with small convergent angle (nanobeam diffraction mode). At this condition, a much better spatial resolution compared to conventional selected area diffraction pattern (SADP) is obtained. Combined with a modern-day fast reading pixelated CMOS camera and post-scan process done by TopSpin software (NanoMEGAS), by scanning across the specimen, one can obtain an EBSD-like orientation map at the nanoscale.

3. Results and discussion

3.1. Microstructure before mechanical tests

The Inverse Pole Figure images of specimen and XRD pattern before compression testing are illustrated in Fig. 1(a) and (b). The peak signal of solution precipitates γ'-(Ni, Fe, Co)$_3$(Al, Ta) is overlapped with the intense signal generated by γ matrix or is annihilated by the strong texture, thereby requiring further characterization to confirm its presence. The initial microstructure was characterized as polycrystalline FCC matrix with a grain size of approximately 400 μm. From the EDS results (Fig. 1(c)), it can be seen that all five elements, except boron, are evenly distributed and incorporated into the matrix phase with no observable intermetallic phase or martensite. Although no pronounced phase segregation was found, the absence of second phase formation is possibly caused by the restriction of step size in EBSD detectors. Fig. 1(d) displays a TEM bright-field micrograph of nano-scale precipitates; the fast Fourier transformation (FFT) diffraction patterns of selected areas are shown in Fig. 1(f) and (g). The corresponding FFT pattern in the red box resolves the formation of ordered $L1_2$-type precipitates phase by displaying the reflection spots of {100} in the interval space between matrix diffraction spots, suggesting a superlattice structure resulting

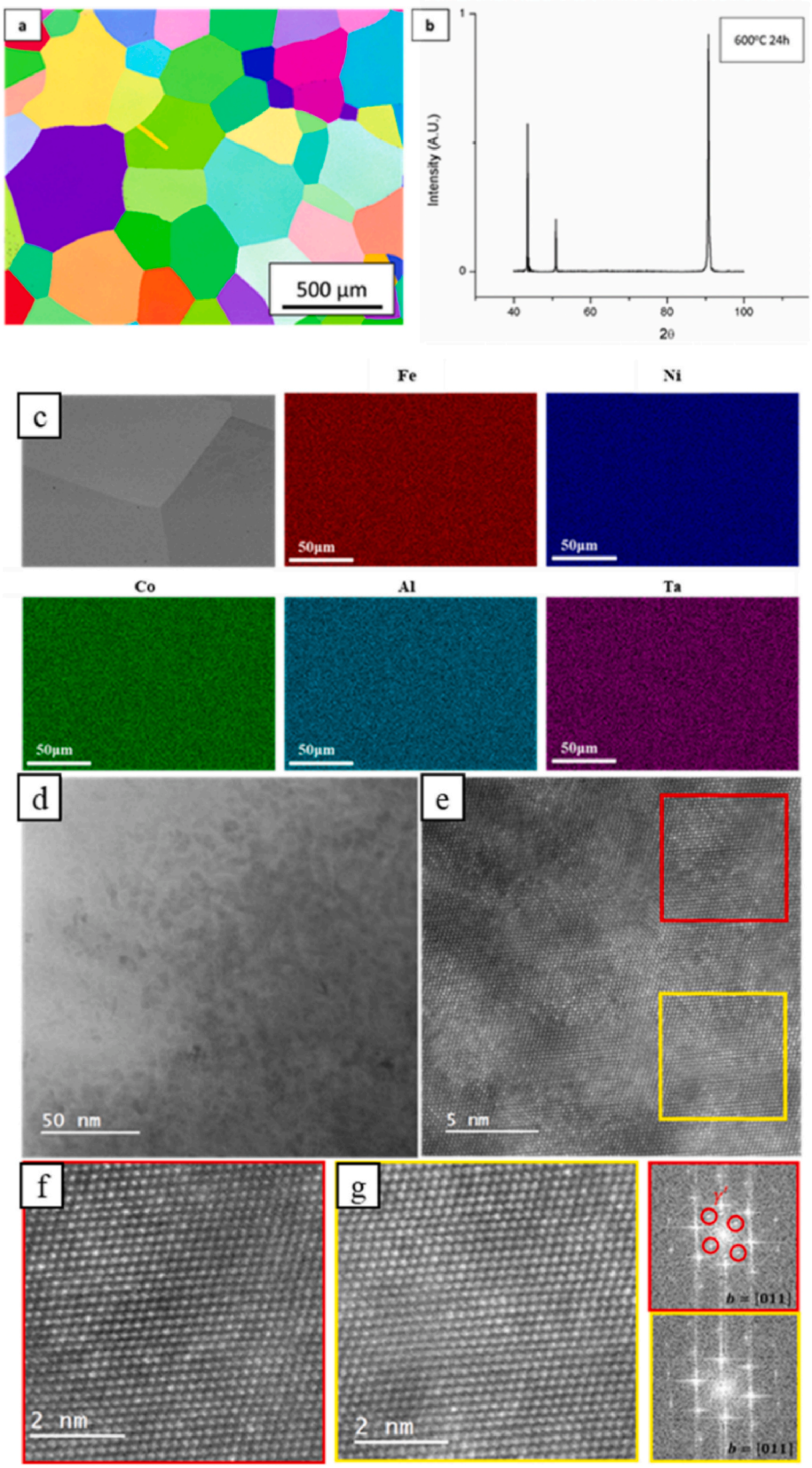

Fig. 1. Microstructure of Fe–Ni–Co–Al–Ta–B HEA before deformation. (a) EBSD inverse pole figure (IPF) of Fe–Ni–Co–Al–Ta–B after hot rolling with reduction in thickness of 30 % and aging at 600 °C for 24h, showing coarse grains with average size around 400 µm and random grain orientation. (b) XRD patterns for aged Fe–Ni–Co–Al–Ta–B HEA, showing single FCC phase. Microstructure of aged samples before deformation. (c) SEM (BSE) micrograph and related EDS mapping results of aged Fe–Ni–Co–Al–Ta–B alloy, showing no element segregation. (d) STEM micrograph of aged Fe–Ni–Co–Al–Ta–B, showing a high density of nano-scale particles; (e)(f)(g) HRTEM micrograph and related FFT images of aged Fe–Ni–Co–Al–Ta–B, confirming the existence of coherent $L1_2$ γ' precipitates (red box) in the FCC matrix (yellow box).

from the ordered γ′ precipitate. The small lattice mismatch (~0.17 % [9]) between γ′ and matrix, and ultra-fined size of precipitate contribute to the nucleation of a highly coherent second phase [52]; this has been shown to be strongly related to the martensite start temperature (M_s) for iron-based alloys [53,54]. Nevertheless, given a prolonged aging treatment, loss of coherency will eventually take place as a consequence of expanding precipitate size. In addition, NiAl–B2 grain-boundary precipitates, which were previously reported by Zhang et al. [55] and regarded as the primary reason for their reported strength and ductility trade-off, were not noticeable in SEM and TEM micrographs.

3.2. Mechanical behavior

Fig. 2 summarizes the compression true stress-true strain curves of FeNiCoAlTaB at three strain rates. For the strain rates of 10^{-3}/s and 10^{-2}/s, the yield strengths (~900 and 950 MPa) show no pronounced difference, and the changes in flow stress corresponding to rising plastic strain are also comparable. However, these results reveal a significant increase in yield strength (~1300 MPa) when subjected to dynamic loading, in comparison with classic CoCrFeMnNi [15] and $Al_{0.3}$CoCrFeNi [17] HEAs. The observed high yield strength indicates the influence of solid solution strengthening, precipitation hardening effects, and potential phase transformations. Quantitative analysis of each strengthening mechanism is presented in Section 4.3, offering detailed insights.

4. Discussion

The present alloy demonstrates both high strength and remarkable work hardening ability, suggesting its significant resistance to thermal softening. This is achieved through the activation of multiple strengthening mechanisms. The dynamic loading-induced deformation mechanisms are thoroughly discussed in Section 4.1, while Section 4.2 addresses shear localization. To investigate the deformation mechanisms under various loading conditions, cylindrical specimens were subjected to uniaxial compressive strains of 0.05, 0.1, and 0.15, while hat-shaped specimens experienced shear strains of 4 and 6.

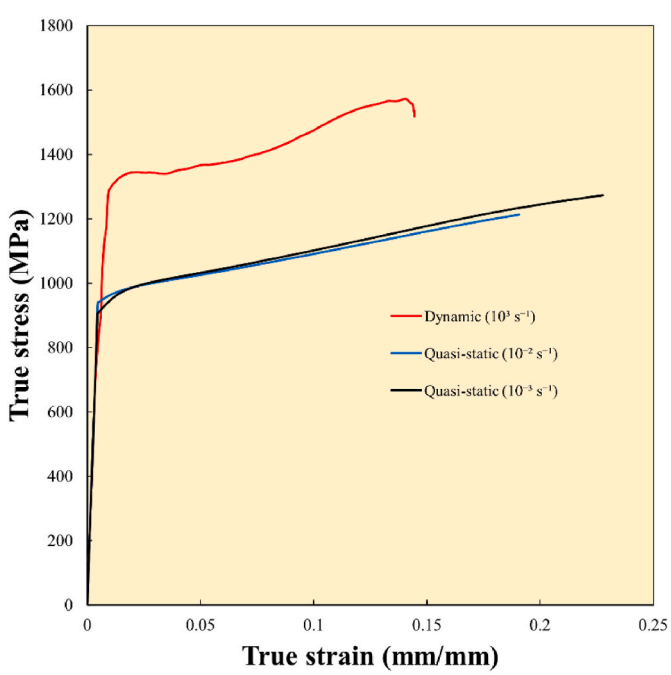

Fig. 2. True stress-true strain curves at three strain rates.

4.1. Deformation mechanisms in FeNiCoAlTaB

4.1.1. Microband strengthening

Fig. 3 illustrates the presence of deformation-induced microbands after a dynamic compressive strain of 0.05, with corresponding line measurement of misorientation. Such low-angle misorientation (~10°) (Fig. 3(b) and d) detected within the banded substructure is considered a typical sign of microband, ruling out the possibility of twinning (misorientation angle ~60°). As the specimens are further strained, TEM reveals the microbands composed of a double-walled structure and intense planar glide on slip plane with a linear array dislocation configuration (Fig. 3(f)). Strong dislocation glide is also verified in Fig. S2, which shows a Taylor lattice formed from strong planar glide on the primary slip system and intersecting dislocations caused by secondary slip [56,57]. At a higher true strain of 0.15, microbands became broader and denser due to the rise of total dislocation density. These double-walled structures consist of localized geometrically-necessary dislocations with a density of 10^{14} m^{-3}, as shown in Fig. 3(e); their widths are ~50 μm. Therefore, microbands not only carry plasticity and accommodate dense dislocation formation but also serve an important role in strain hardening via generating impenetrable walls that hinder the dislocation movement [58]. Interestingly, no pronounced dislocation cells resulting from cross-slip, which are common dislocation configurations in high SFE materials, were observed. Considering the inherent high SFE of this alloy [9], whose plastic deformation is controlled by microband and dislocation glide, this seemingly contradictory phenomenon is ascribed to so-called "glide plane softening" effect [59], demonstrating that slip mode in FCC solid solution alloys is governed by planar glide due to presence of short-range ordering in concentrated solid solution alloys (including HEAs), regardless of SFE. However, short-range ordering in HEAs has yet to be unequivocally demonstrated via experimental and theoretical studies. Some recent work claims to discover such an effect mainly through microscopy and characterize its influence on the mechanical properties [60–62]. However, the validity of their appearance in high-entropy alloys has received considerable criticism and requires further proof. Meanwhile, there is little evidence that short-range ordering can tailor the mechanical properties at the macroscale due to its small degree [63,64]. In addition, other than SFE and local chemical ordering, strain rate, grain size, and deformation mode also play important roles in dislocation glide mode [65]. Their combined effects on glide mode require further investigation.

We suggest that the extensive microbanding occurs as a result of two factors: the inherently high SFE of current alloy, and the coarse grains, which are beneficial to the development of a heterogeneous dislocation substructure [66]. TEM and EBSD displayed strong planar glide and linear arrays of dislocations, which are widely believed to be precursors to microbanding.

4.1.2. Stress-induced martensitic transformation

Characterization of stress-induced martensitic transformation was performed at various levels of strain to further investigate its source and effect on dynamic properties. EBSD coupled with TEM (Fig. 4) show the microstructures of specimen after a dynamic compressive strain of 0.05. The intersecting needle-like features (see Fig. 4(a) and (b)) were identified as BCC structures under TEM, and the corresponding FFT pattern (blue box) indicates a martensitic transformation with the Greninger-Troiano (G-T) relationship ($(110)_{\alpha'} \parallel (111)_{\gamma}$) [67].

It is also revealed in two sets of FFT patterns (Fig. 4(d)(f)) that the martensite possesses two different variants, indicating a region comprised of intersecting thin plates. Accordingly, the onset of phase transformation occurred when strain was below 0.05. This finding agrees well with the results reported by Tanaka et al. [42], who claimed a superb superelasticity in Fe–Ni–Co–Al–Ta–B alloy achieved via recovery of stress-induced BCC/BCT martensite, hence the formation of martensite at a small strain. The initiation of stress-induced martensitic

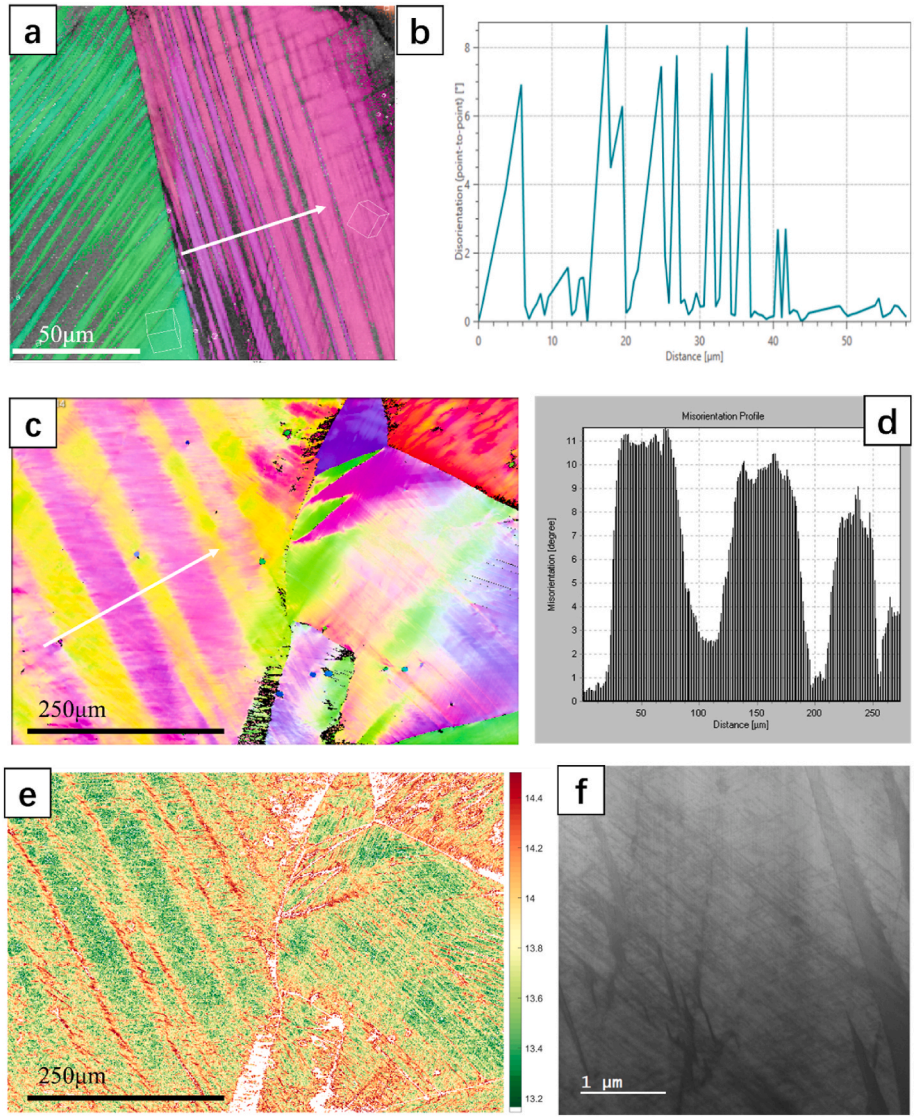

Fig. 3. EBSD IPF mapping of aged Fe–Ni–Co–Al–Ta–B alloy with dynamic compressive strain of (a) 0.05 and (c) 0.15, showing the existence of deformation-induced microbands, and their corresponding misorientation profile (b,d) along direction marked with white arrow. (e) Calculated geometrically-necessary dislocation density (GND) (m^{-2}) distribution map corresponding to (c), indicating that higher GND density (10^{14} m^{-2}) is located along the boundaries of microbands. (f) TEM bright-field micrograph displaying strong planar glide and intersecting microbands at compressive strain of 0.15.

transformation is associated with a critical stress σ_{crit}, representing how much external loading must be applied to overcome the free energy barrier between austenite and martensite phases. The value of σ_{crit} is closely related to the stability of parent phase; the stabilized austenite matrix requires a higher critical stress to achieve phase transition. In the coarse-grained (~200 μm) alloy aged at 700 °C for 24h, σ_{crit} was established to be 510 MPa [68] in quasi-static loading. Although a sufficiently high yield stress (1300 MPa) was obtained in dynamic deformation, we must not overlook the effect caused by the elevated strain rate. On the basis of Olson and Cohen's theory [69], both coherency and misfit dislocations are required for the nucleation of martensite. Therefore, the change in trigger stress of martensite formation caused by elevated strain rate, although not precisely measured in the current work, is mainly governed by irreversible work consumed in overcoming internal frictional resistance during phase interface movement [70,71]. Due to both thermal activation and phonon drag effects, rising strain rate is usually coupled with enhanced resistance to dislocation movement along phase boundaries between matrix phase and induced martensite, hence the increased trigger stress.

The identification of stress-induced phase transformation in dynamically deformed Fe–Ni–Co–Al–Ta–B is also supported by the observation of martensite in quasi-statically deformed specimens at a strain smaller than 0.005 and stress level of below 1000 MPa (see Fig. S3). There is no temperature rise when the specimen is subjected to quasi-static loading. It has been demonstrated that this alloy's onset of martensitic transformation is stress-related rather than strain-related [42,72–74].

As strain increases, BCC martensite's volume fraction (measured using the manual point count method based on the ASTM E562 [75] combined with EBSD phase mapping) increases significantly. The transformation rate ($dV_{\alpha'}/d\varepsilon$) and volume of martensite unit are used here to describe the kinetics of stress-induced martensitic transformation. Additional quantification was conducted to understand the kinetics of martensitic transformation at different strain rates. The volume fraction of martensite, $V_{\alpha'}$, as a function of true plastic strain, ε_t, can be expressed by the equation proposed by Guimarães [76]:

$$V_{\alpha'} = 1 - \exp\left(-k\varepsilon_t^{z}\right) \quad (1)$$

where k and z are material constants. Eq. (1) has the same form as the

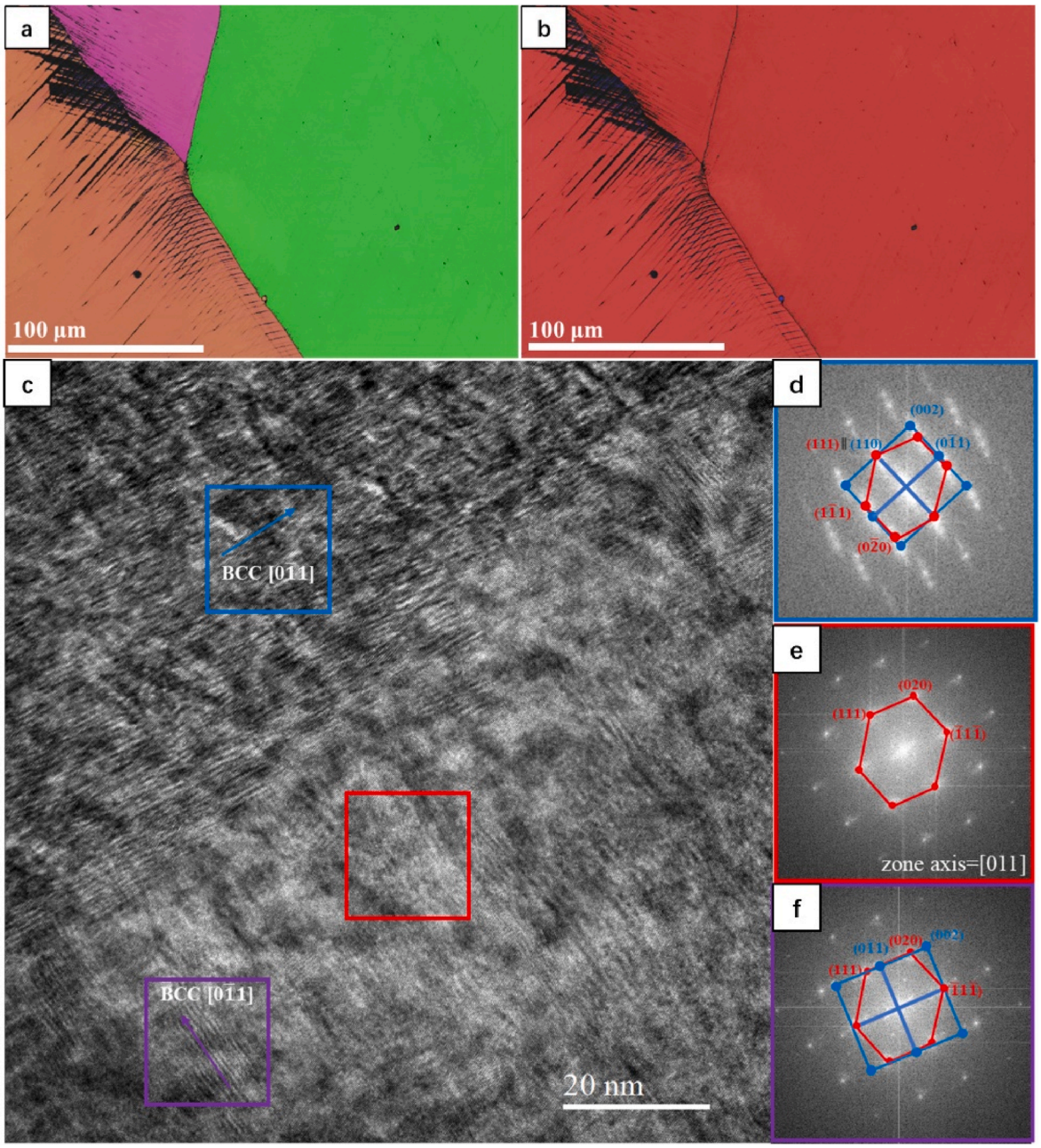

Fig. 4. Formation of BCC/BCT α' martensite in dynamically deformed specimen at true strain of 0.05. (a) IPF and (b) phase mapping reveals the stress-induced martensite at the vicinity area of grain boundaries with thin-plate morphology. (c) TEM micrograph and corresponding FFT diffraction pattern resolving (d) FCC to BCC/BCT martensitic transformation following G-T relationship and (e) FCC matrix. (f) FFT pattern indicating secondary variant of martensite.

Johnson-Mehl-Avrami-Kolmogorov equation; in the latter, the fraction of material that is transformed is expressed as a function of time. The Guimarães equation in Fig. 5 replaces time by strain. The values of k and z are obtained by fitting the experimental data points shown in Fig. 5(a). Based on the fitted results, the parameters of Eq. (1) are k~1.479 and z~0.824. One exceptionally high-volume martensite fraction was observed at a true strain of 0.10. The corresponding EBSD phase map (Fig. S4) suggests that such abnormal phenomenon can be attributed to ultra-coarse grain (~1 mm), hence the exclusion in the fitted data. The martensite volume fraction at high strain ($\varepsilon = 70\%$) was obtained by conducting quasi-static compression on an encapsulated cylinder specimen (as shown in Fig. S5). The confinement by the capsule enabled recovery after the fracture strain. A high martensite formation rate $dV_{\alpha'}/d\varepsilon$ is expected at the early stage of deformation (Fig. 5(b)) due to the initially large austenite grains. As plastic strain continues to rise, the transformation rate gradually decreases [77]. The continuously decreasing transformation rate is explained schematically in Fig. 5(c). The initial nucleation of first martensite plates is mainly governed by the pre-existing nucleation sites which are primarily along the grain boundaries and strongly dependent on the grain size. However, the subsequent growth of martensite is heavily constrained to the retaining austenite matrix which is refined by the growth of the first plates. The divided and strained pockets austenite matrix generate strain fields in surrounding areas, resisting the propagation of subsequent martensite plates [78].

4.2. Dynamic deformation and shear localization

Although multiple strengthening effects operate in dynamically compressed cylindrical specimens, a steadily decreasing strain

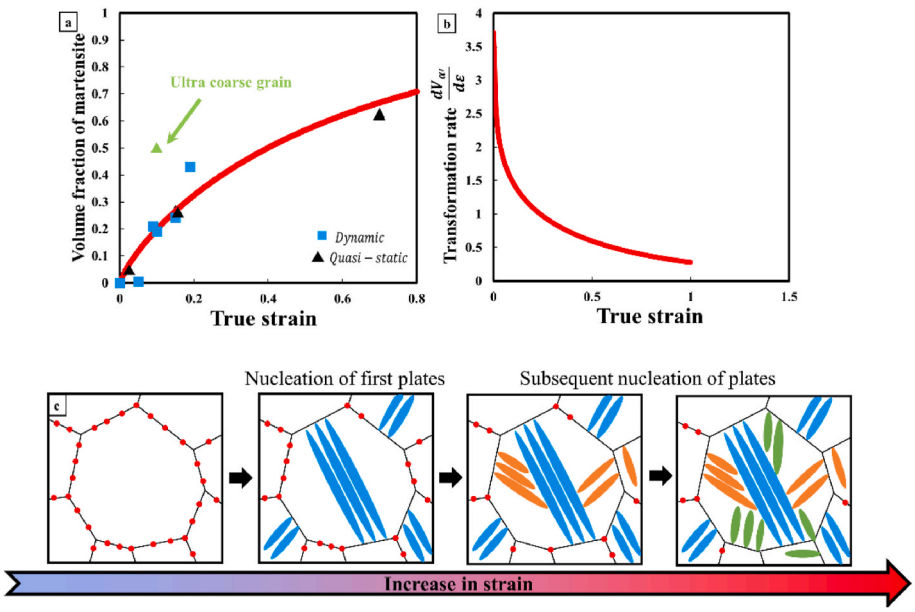

Fig. 5. (a) Volume fraction of martensite as a function of true plastic strain. Fit to Guimarães equation (Eqn. (1)) in red curve. Blue, green, and black data points are experimentally obtained. (b) Martensite transformation rate ($dV_{\alpha'}/d\varepsilon$) as a function of true strain. The transformation rate starts at true strain close to zero. (c) Schematic representation of increasing martensite transformation with increasing strain.

hardening rate and temperature rise predispose the structure to shear localization. The dynamically compressed hat-shaped specimens generate significantly higher strains than the cylindrical specimens.

Fig. 6(a) shows two shear stress vs. shear strain curves. The irregularities are mainly attributed to the nature of wave propagation in the Hopkinson bar. EBSD micrographs of hat-shaped specimens with a shear strain of 4 are shown in Fig. 6(c and d); no visible shear banding is observed. Strain and misorientation localize in the shear zone area, as shown in Fig. 6(c) and (d), and the region in the vicinity of the shear zone experiences less deformation. In addition, the localized strain is aligned with the shear direction, suggesting a preliminary stage of shear banding. For a shear strain of 6, Fig. 6(e, f, g), pronounced shear localization coupled with poor band contrast was observed. The poor mapping quality in the internal domain of shear band is due to the limitation of minimum step size of EBSD detector. This is suggestive of nanometer-sized grains. Thus, the critical shear strain to initiate shear localization is estimated to be between 4 and 6. This phenomenon is consistent with the corresponding shear stress vs. shear strain curves for a maximum of 6; it exhibits a rapid drop of strain hardening rate at a shear strain of approximately 5. The imposed work done during the dynamic shearing test can be converted to the temperature rise ΔT, within the shear zone through the following expression:

$$\Delta T = \frac{\beta}{\rho C_P} \int \tau d\gamma \tag{2}$$

where τ and γ are shear stress and strain, respectively, $\rho \sim 7900 kg/m^3$ (estimated through the classic mixing rule) is the density, $C_p \sim 442.29 J/(kg \bullet K)$ is the specific heat capacity acquired from the weight average method, and β is the Taylor-Quinney coefficient, which expresses the efficiency of plastic work to heat conversion. Determination of the Taylor-Quinney coefficient β is difficult both theoretically and experimentally, since it is dependent on various factors, including deformation mechanisms, dislocation substructures, temperature, composition and grain size. β is universally set to be 0.9 when deformation is the result of dislocation movement, suggesting that majority (90 %) of the mechanical work is converted to heat and only a minor part (10 %) of the work is stored as strain energy (primarily, dislocations). However, the temperature rise obtained is as high as 1600 K (as shown in Fig. 6(a)), leading to a total temperature above the melting point of Fe–Ni–Co–Al–Ta–B ($T_m \sim 1708$ K), which is theoretically not possible. Values of β far below 0.9 have been found in Al alloy [79] and CoCrFeMnNi alloy [80]. This has been attributed to more plastic work being stored in the microstructures. The evolution of martensitic transformation can significantly affect the energy storage mechanisms [79,81]. There are complications, such as formation of martensite being coupled with the release of latent heat, in some cases [66]. Thus, the lower Taylor-Quinney coefficient in the current alloy can be plausibly attributed to non-uniform deformation and extraneous effects [82].

Fig. 7(a) is the TEM micrograph of the region inside the shear band; the corresponding selected area diffraction pattern (SADP) is shown in Fig. 7(b). The grain sizes within the shear band mostly range from 50 to 100 nm, which can also be confirmed by the corresponding TEM-based PED result (Fig. 7(d)). These equiaxed nano grains result from rotational dynamic recrystallization and are substantially smaller than the initial coarse grain size ($\sim$400 μm). The mechanism of rotational dynamic recrystallization, first postulated by Meyers et al. [83], is described in depth by Yan et al. [84]. The SADP pattern exhibits a continuous sharp ring, negating the presence of an amorphous phase; the respective planes corresponding to the rings were determined from the d-spacing. Unsurprisingly, both deformation-induced microband and stress-induced martensite are present. However, the TEM-based PED phase map (Fig. 8(a)) shows that some of this martensite locates within the fine-grain area. The joint effects of the drastic temperature rise and grain refinement lead to the change in critical stress to initiate phase transition.

4.3. Multiple strengthening mechanisms

The stress-strain curve for the dynamically deformed specimen shown in Fig. 2 reveals that there is an excellent synergy of strength and ductility. The outstanding mechanical properties are associated with multiple strengthening mechanisms: precipitation, solid solution, microbands, and martensitic transformation strengthening.

Recognizing that this estimation is likely to result in a significant overestimation, we can approximate an upper bound for the total contribution derived from various strengthening mechanisms as follows:

$$\sigma_{total} \approx \sigma_0 + \sigma_p + \sigma_{GB} + \sigma_{ss} + \sigma_M + \sigma_{MB} \tag{3}$$

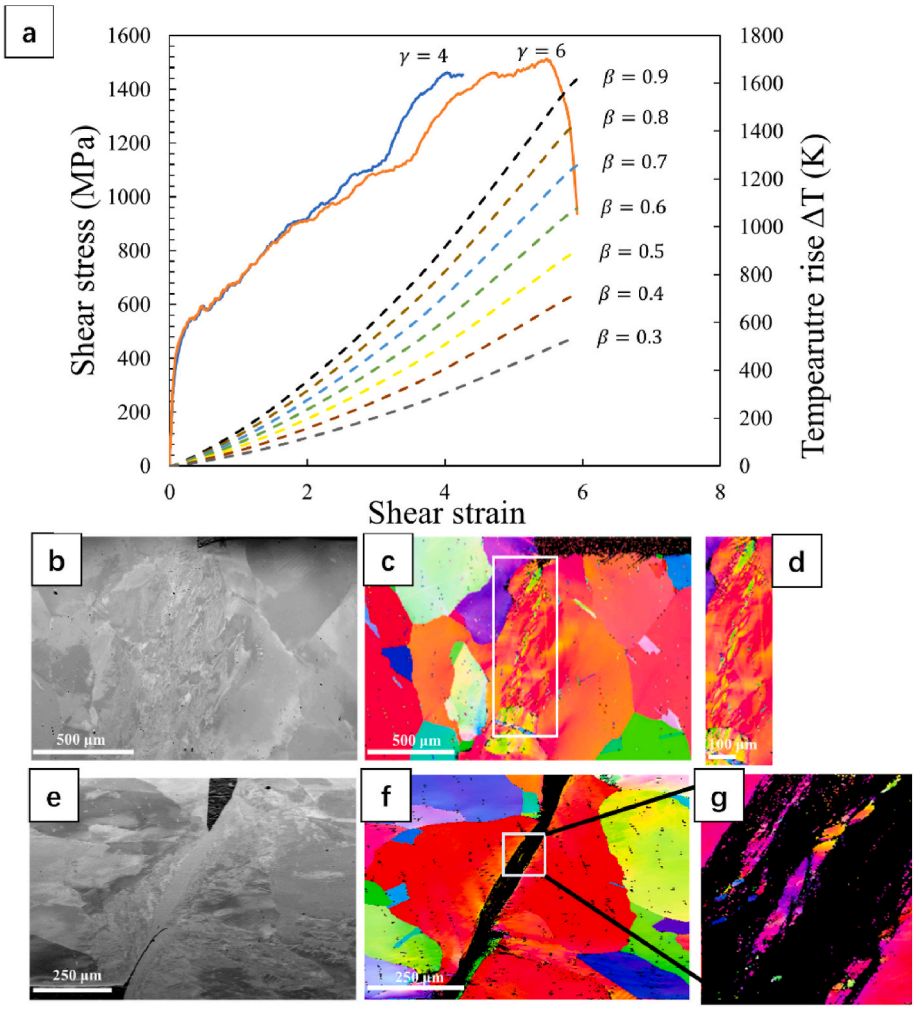

Fig. 6. Mechanical properties and microstructural characterization of hat-shape specimens. (a) Shear stress τ as a function of shear strain γ and the corresponding temperature rise acquired from different β values (=0.3, 0.4, 0.5, 0.6, 0.7, 0.8, 0.9). Forward scatter detector (FSD) images and EBSD IPF maps of hat-specimens that experienced shear strains of (b, c, d) 4 and (e, f, g) 6.

where σ_0 is lattice friction force (we here use 141 MPa), σ_p is precipitation strengthening, σ_{GB} is grain-boundary strengthening derived from the Hall-Petch equation, σ_{ss} represents the contribution to strength from solid solution strengthening, σ_M is the stress contribution caused by martensitic transformation, and σ_{MB} is microband strengthening. The first four strengthening effect mechanisms (σ_0, σ_p, σ_{GB}, σ_{ss}) are classic and common to many HEAs. The last two (σ_M, σ_{MB}) are exclusive of the alloy studied here. It has to be mentioned that this is a simplification: the strengthening effects are not simply additive. The solid solution strengthening effect, precipitation hardening, lattice frictional stress, and grain-boundary strengthening are considered to be independent of plastic deformation. Dislocation hardening, martensite strengthening and microband strengthening, however, strongly rely on plastic strain and influence the work hardening and strain rate dependence of flow stress significantly.

The conventional precipitation strengthening effect by coherent $L1_2$-γ' acts by forming interfaces between matrix and precipitates, thereby impeding dislocation movement [85]. In the present alloy, due to retained coherency between matrix and $L1_2$-γ' with a fine particle size (~4 nm [86]), the operative strengthening mechanism is classified as dislocation-shearing [87]. Accordingly, the contribution to yield stress originated from nano-scale γ' precipitates can be quantified by Ref. [88]:

$$\sigma_p = 0.81M\left(\frac{\gamma_{APB}}{2b}\right)\left(\frac{3\pi f_{\gamma'}}{8}\right)^{\frac{1}{2}} \tag{4}$$

where M is Taylor factor (3.06 for polycrystalline FCC materials), $f_{\gamma'}$ is volume fraction of γ' particles (~0.38 for 600 °C 24h aged NCATB HEA [89]), b is the magnitude of the Burgers vector (0.254 nm), and γ_{APB} is anti-phase boundary energy (0.11 J/m^2) [90,91]. This contribution is $\sigma_p \sim 359$ MPa. Due to the small amount of B2 precipitates found, their contribution to total stress will not be included in our calculations.

The stress contribution by grain size strengthening is expressed by Ref. [92]:

$$\sigma_{GB} = k_y d^{-0.5} \tag{5}$$

Where k_y is strengthening coefficient (440 MPa μm$^{0.5}$ [8]), d is grain diameter ~ 400 μm. By substituting these values into Eq. (5), we obtain $\sigma_{GB} = 22$ MPa. Therefore, due to the coarse grains, grain size strengthening is minimal.

In addition, solid solution strengthening can be described by the solid solution model developed by Varvenne et al. [93,94]. This model is specifically developed to predict yield strengths in FCC HEAs and can be expressed as:

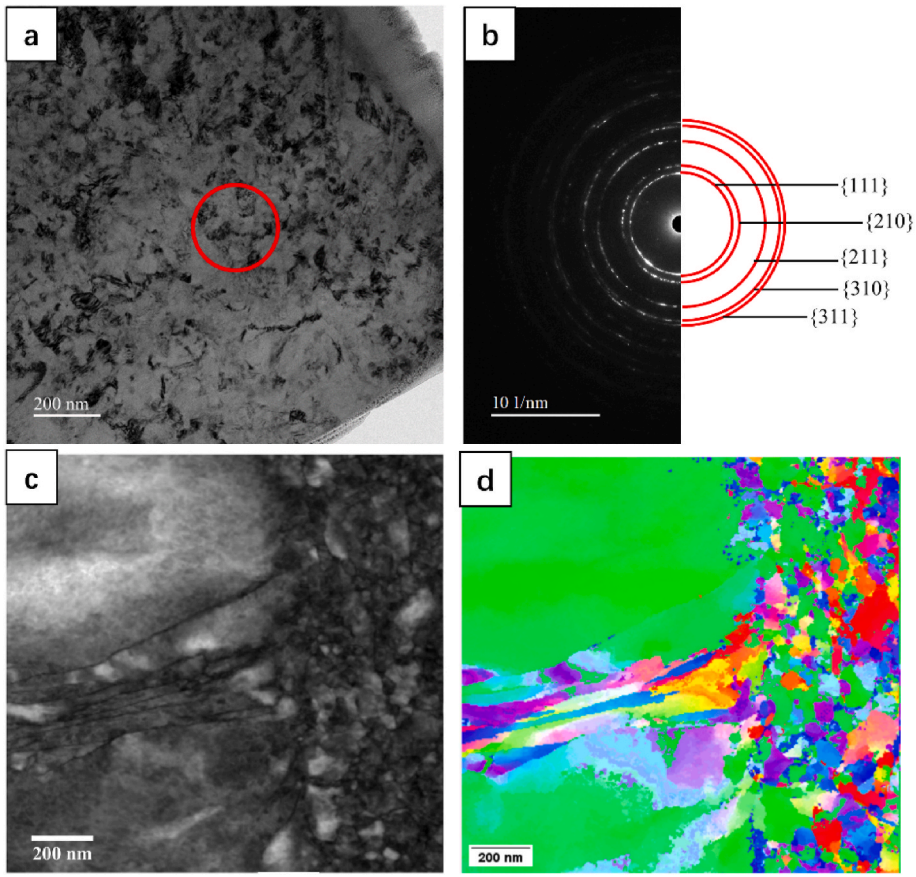

Fig. 7. (a) Bright-field TEM micrograph of microstructure within shear band. (b) SADP pattern of area within red circle, illustrating formation of nanograins formation with various orientation. (c) TEM-based PED map showing boundary between coarse grain and nanograin and its corresponding (d) IPF map.

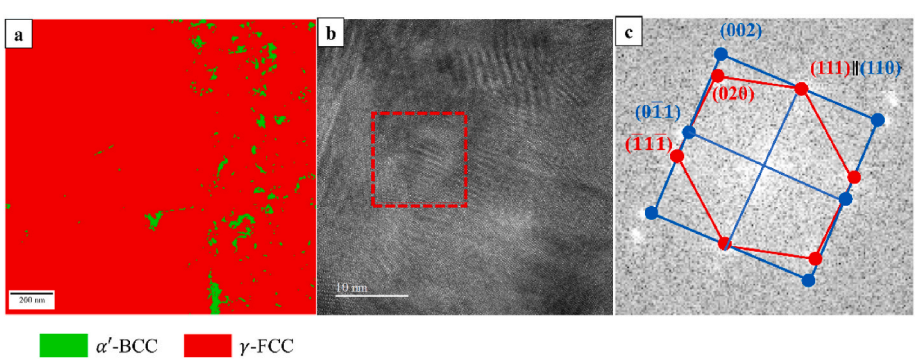

Fig. 8. (a) TEM-based PED phase map showing distribution of α'-BCC (green) and γ-FCC (red). (b) TEM micrograph within ultra-fine grain area and its corresponding (c) FFT pattern, resolving formation of martensite within shear band.

$$\sigma_{ss} = 0.01785\left(1 - f_{\gamma'}\right)\alpha^{-\frac{1}{3}}\overline{G}\left(\frac{1+\overline{\nu}}{1-\overline{\nu}}\right)\left[\frac{\sum_n c_n \Delta V_n^2}{b^6}\right]^{\frac{2}{3}} \tag{6}$$

$\overline{G}$ and $\overline{\nu}$ represent average elastic constants, α (~0.123) is a temperature-independent edge dislocation line tension coefficient, ΔV_n are misfit volumes and c_n is the atomic fraction of element n. Since the original equation is only applicable for random solution alloy, the effect of the volume fraction ($f_{\gamma'}$ ~ 38 %) of ordered γ' phase was taken into account by multiplying the final results by a correction factor $(1 - f_{\gamma'})$. Hereafter, we obtained an increment in the yield stress σ_{ss} as high as 465 MPa.

The sum of σ_{GB}, σ_p, σ_0, and σ_{ss} predicts a yield strength of 987 MPa, slightly higher than the yield strength (900 MPa) measured in quasi-static compression. There are several reasons for the difference, one primary explanation is the overlapped strengthening effect in this alloy, whereas we here consider each strengthening is independent and contributing fully to the total stress.

The strain hardening contributed by microbands can be divided into two components, namely forest strengthening, and the hardening effect derived from enhanced stress to transfer plasticity across dislocation boundaries. The strengthening effect can be specifically acquired from substructures containing high dislocation density, which can be represented as [95,96]:

$$\sigma_{Taylor} \approx M\alpha Gb\rho^{0.5} \tag{7}$$

$$\sigma_{Transfer} \approx Gb\left(\frac{\theta}{\delta b}\right)^{0.5} \tag{8}$$

where G is the shear modulus (~77 GPa), α is forest interaction parameter 0.3, b is the Burgers vector (~0.254 nm), M (~3.06) is the Taylor factor, θ is the misorientation angle (~10° from misorientation profile), δ is mean spacing of microbands (~50 μm) and ρ is dislocation density in cell wall (~$10^{14}/m^2$) (as shown in Fig. 3(e)). Eq. (7) represents Taylor's strengthening effect in the wall structure of microbands and the increasing stress required to transfer plasticity through them. Eq. (8) is the strengthening effect caused by grain misorientation. As local shear strain continues to accumulate, the misorientation angle, θ, increases, leading to thickened cell structures which help to impede dislocation migration [97]. By substituting this parameter into Eqns. (7) and (8), the following values emerge: $\tau_{Taylor} \approx 180MPa$ and $\tau_{Transfer} \approx 73MPa$. It has also been reported that microbands are a desired deformation mechanism to overcome the traditional strength-ductility trade off ([97,98]). The optimized ductility is mainly associated with dislocation-deficient areas between microbands which are shown in the GND analysis (Fig. 3(e)). This strengthening effect is also depicted as hetero-deformation induced hardening by Zhang and Zhu [99] for Fe–Ni–Co–Al–Ta–B HEA. Therefore, we assume that the excellent work hardening ability and ductility are contributed by microbands in dynamic compression.

The formation of martensite within the austenite matrix can enhance the flow stress in two manners: (1) the formation of second phase can provide interface boundaries for dislocation accumulation [100]; (2) the intrinsically harder BCC phase exhibits better strength against external loading than the FCC phase [101]. We here determine the enhanced stress based on the latter theory. Therefore, the increment in stress caused by martensite phase formation can be expressed by classic mixing rule [102,103]:

$$\sigma_M \approx V_{\alpha'}\sigma_{\alpha'} - V_{\alpha'}\sigma_{\gamma} \tag{9}$$

where $\sigma_{\alpha'}$ and σ_{γ} are strength of α' martensite and γ matrix phase. We here use the Vickers hardness of martensite (~600 HV [104]) and austenite matrix composed of nanoprecipitates (~430 HV [73]) to approximate their corresponding strength ($\sigma_y \sim 3H_V$). By substituting these parameters, we obtain σ_M ~163 MPa, which is smaller than the value derived from microband strengthening.

In summary, multiple strengthening effects, including solid solution strengthening, transformation strengthening, microband strengthening and precipitation strengthening, likely contribute to the excellent mechanical behavior of NCATB when deformed under dynamic conditions.

5. Conclusions

We report on a high performance, aged Fe–Ni–Co–Al–Ta–B alloy with excellent dynamic yield strength and adequate deformability. We evaluated the phase transformation mechanisms in the aged Fe–Ni–Co–Al–Ta–B alloy. The volume fraction of martensite increases significantly during deformation. The inherently high SFE of the current alloy inhibits twinning while microband formation governs plastic deformation. The combined effects of stress-induced martensitic transformation and deformation-induced microbanding provide an excellent resistance to shear localization with a γ_{crit} higher than 4.

The microstructure evolution in the dynamically deformed Fe–Ni–Co–Al–Ta–B alloy is schematically illustrated in Fig. 9. Comparison of the various strengthening mechanisms suggests that the excellent yield strength of aged alloy is primarily attributable to two factors: solution and precipitation strengthening. The high yield stress provides the required driving force to the onset of stress-induced martensitic transformation during elastic deformation. A thin-plate martensite phase was observed even under conditions of a small degree of elastic deformation; however, due to its limited volume fraction, any property enhancement derived from the phase transition was deemed negligible. As the strain level continues to increase, due to strong planar glide in the alloy, the deformation-induced microbands form to carry plasticity and provide the dominant strengthening effect. The continuous development of microbands promotes some ductility and sustains the growth of martensite. The interaction between phase transition and microbanding leads to the development of intersecting thin-plate martensite and microbands. Despite extensive microbanding and martensitic transformation, the strain hardening capacity is eventually overwhelmed by the thermal softening effect due to intense shear deformation. This phenomenon gives rise to shear instability which leads to localization and ultra-fine grains formed by a rotational recrystallization mechanism.

CRediT authorship contribution statement

Aomin Huang: Writing – original draft, Formal analysis, Methodology. **Cheng Zhang:** Conceptualization, Formal analysis, Investigation, Methodology, Validation, Writing – review & editing. **Zezhou Li:** Formal analysis, Writing – review & editing. **Haoren Wang:** Formal analysis, Investigation. **Mingjie Xu:** Investigation, Formal analysis. **Chaoyi Zhu:** Formal analysis. **Xin Wang:** Formal analysis, Investigation. **Marc A. Meyers:** Conceptualization, Methodology, Funding acquisition, Formal analysis, Validation, Writing – review & editing.

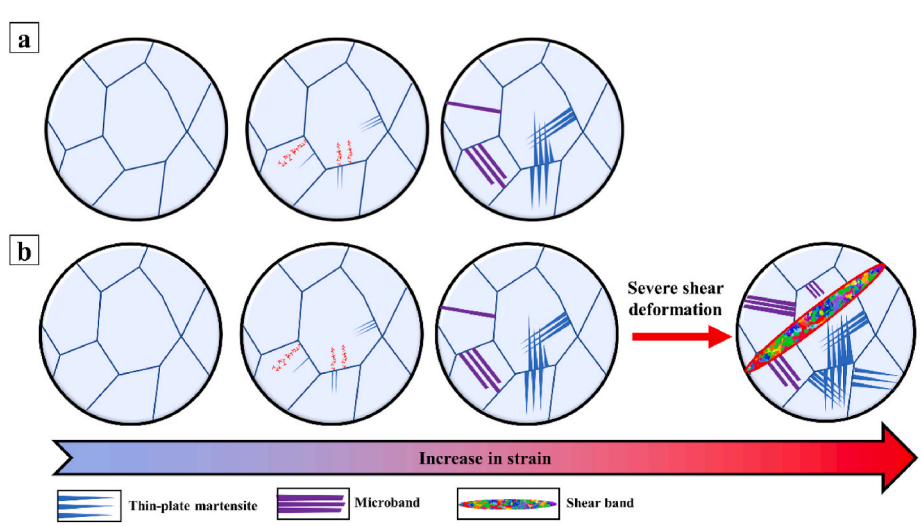

Fig. 9. Schematic diagram illustrating the microstructural evolution of Fe–Ni–Co–Al–Ta–B alloy with increasing strain during (a) quasi-static and (b) dynamic deformation.

Enrique J. Lavernia: Conceptualization, Methodology, Funding acquisition, Project administration, Formal analysis, Validation, Writing – review & editing.

Declaration of competing interest

The authors declare that they have no known competing financial interests or personal relationships that could have appeared to influence the work reported in this paper.

Data availability

Data will be made available on request.

Acknowledgements

Fruitful discussions with Prof. K. S. Vecchio are gratefully acknowledged. C.Z., X.W., and E.J.L. would like to acknowledge the financial support from UCI and TAMU. This research (X.W. and E.J.L.) was partially supported by the National Science Foundation Materials Research Science and Engineering Center program through the UC Irvine Center for Complex and Active Materials (DMR-2011967). C.Z., X. W., M.X., and E.J.L. also acknowledge the use of facilities and instrumentation at the UC Irvine Materials Research Institute (IMRI), which is supported in part by the National Science Foundation through the UC Irvine Materials Research Science and Engineering Center (DMR-2011967).

Appendix A. Supplementary data

Supplementary data to this article can be found online at https://doi.org/10.1016/j.mtadv.2023.100439.

References

[1] J.W. Yeh, S.K. Chen, S.J. Lin, J.Y. Gan, T.S. Chin, T.T. Shun, C.H. Tsau, S. Y. Chang, Nanostructured high-entropy alloys with multiple principal elements: novel alloy design concepts and outcomes, Adv. Eng. Mater. 6 (2004) 299–303, https://doi.org/10.1002/adem.200300567.

[2] E.P. George, D. Raabe, R.O. Ritchie, High-entropy alloys, Nat. Rev. Mater. 4 (2019), https://doi.org/10.1038/s41578-019-0121-4.

[3] D.B. Miracle, O.N. Senkov, A critical review of high entropy alloys and related concepts, Acta Mater. 122 (2017) 448–511, https://doi.org/10.1016/j.actamat.2016.08.081.

[4] B. Gludovatz, A. Hohenwarter, D. Catoor, E.H. Chang, E.P. George, R.O. Ritchie, A fracture-resistant high-entropy alloy for cryogenic applications, Science 345 (2014) 1153–1158, https://doi.org/10.1126/science.1254581.

[5] D. Liu, Q. Yu, S. Kabra, M. Jiang, P. Forna-Kreutzer, R. Zhang, M. Payne, F. Walsh, B. Gludovatz, M. Asta, A.M. Minor, E.P. George, R.O. Ritchie, Exceptional fracture toughness of CrCoNi-based medium- and high-entropy alloys at 20 kelvin, Science 378 (2022) 978–983, https://doi.org/10.1126/science.abp8070, 1979.

[6] J.Y. He, H. Wang, H.L. Huang, X.D. Xu, M.W. Chen, Y. Wu, X.J. Liu, T.G. Nieh, K. An, Z.P. Lu, A precipitation-hardened high-entropy alloy with outstanding tensile properties, Acta Mater. 102 (2016), https://doi.org/10.1016/j.actamat.2015.08.076.

[7] Y. Tong, D. Chen, B. Han, J. Wang, R. Feng, T. Yang, C. Zhao, Y.L. Zhao, W. Guo, Y. Shimizu, C.T. Liu, P.K. Liaw, K. Inoue, Y. Nagai, A. Hu, J.J. Kai, Outstanding tensile properties of a precipitation-strengthened $FeCoNiCrTi_{0.2}$ high-entropy alloy at room and cryogenic temperatures, Acta Mater. 165 (2019) 228–240, https://doi.org/10.1016/j.actamat.2018.11.049.

[8] Z. Fu, L. Jiang, J.L. Wardini, B.E. MacDonald, H. Wen, W. Xiong, D. Zhang, Y. Zhou, T.J. Rupert, W. Chen, E.J. Lavernia, A high-entropy alloy with hierarchical nanoprecipitates and ultrahigh strength, Sci. Adv. 4 (2018), https://doi.org/10.1126/sciadv.aat8712.

[9] C. Zhang, C. Zhu, P. Cao, X. Wang, F. Ye, K. Kaufmann, L. Casalena, B. E. MacDonald, X. Pan, K. Vecchio, E.J. Lavernia, Aged metastable high-entropy alloys with heterogeneous lamella structure for superior strength-ductility synergy, Acta Mater. 199 (2020) 602–612, https://doi.org/10.1016/j.actamat.2020.08.043.

[10] T. Yang, Y.L. Zhao, Y. Tong, Z.B. Jiao, J. Wei, J.X. Cai, X.D. Han, D. Chen, A. Hu, J.J. Kai, K. Lu, Y. Liu, C.T. Liu, Multicomponent intermetallic nanoparticles and superb mechanical behaviors of complex alloys, Science, 362 (6417) 933-937. https://doi.org/10.1016/10.1126/science.aas8815..

[11] J. Rackwitz, Q. Yu, Y. Yang, G. Laplanche, E.P. George, A.M. Minor, R.O. Ritchie, Effects of cryogenic temperature and grain size on fatigue-crack propagation in the medium-entropy CrCoNi alloy, Acta Mater. 200 (2020), https://doi.org/10.1016/j.actamat.2020.09.021.

[12] O.N. Senkov, G.B. Wilks, D.B. Miracle, C.P. Chuang, P.K. Liaw, Refractory high-entropy alloys, Intermetallics 18 (2010) 1758–1765, https://doi.org/10.1016/j.intermet.2010.05.014.

[13] O.N. Senkov, S. Gorsse, D.B. Miracle, High temperature strength of refractory complex concentrated alloys, Acta Mater. 175 (2019), https://doi.org/10.1016/j.actamat.2019.06.032.

[14] E.P. George, W.A. Curtin, C.C. Tasan, High entropy alloys: a focused review of mechanical properties and deformation mechanisms, Acta Mater. 188 (2020) 435–474, https://doi.org/10.1016/j.actamat.2019.12.015.

[15] Z. Li, S. Zhao, S.M. Alotaibi, Y. Liu, B. Wang, M.A. Meyers, Adiabatic shear localization in the CrMnFeCoNi high-entropy alloy, Acta Mater. 151 (2018) 424–431, https://doi.org/10.1016/j.actamat.2018.03.040.

[16] D.L. Foley, S.H. Huang, E. Anber, L. Shanahan, Y. Shen, A.C. Lang, C.M. Barr, D. Spearot, L. Lamberson, M.L. Taheri, Simultaneous twinning and microband formation under dynamic compression in a high entropy alloy with a complex energetic landscape, Acta Mater. 200 (2020) 1–11, https://doi.org/10.1016/j.actamat.2020.08.047.

[17] Z. Li, S. Zhao, H. Diao, P.K. Liaw, M.A. Meyers, High-velocity deformation of $Al_{0.3}CoCrFeNi$ high-entropy alloy: remarkable resistance to shear failure, Sci. Rep. 7 (2017) 1–8, https://doi.org/10.1038/srep42742.

[18] N. Kumar, Q. Ying, X. Nie, R.S. Mishra, Z. Tang, P.K. Liaw, R.E. Brennan, K. J. Doherty, K.C. Cho, High strain-rate compressive deformation behavior of the $Al_{0.1}CrFeCoNi$ high entropy alloy, Mater. Des. 86 (2015) 598–602, https://doi.org/10.1016/j.matdes.2015.07.161.

[19] J.M. Park, J. Moon, J.W. Bae, M.J. Jang, J. Park, S. Lee, H.S. Kim, Strain rate effects of dynamic compressive deformation on mechanical properties and microstructure of CoCrFeMnNi high-entropy alloy, Mater. Sci. Eng. 719 (2018) 155–163, https://doi.org/10.1016/j.msea.2018.02.031.

[20] K. Jiang, T. Ren, G. Shan, T. Ye, L. Chen, C. Wang, F. Zhao, J. Li, T. Suo, Dynamic mechanical responses of the $Al_{0.1}CoCrFeNi$ high entropy alloy at cryogenic temperature, Mater. Sci. Eng. 797 (2020), 140125, https://doi.org/10.1016/j.msea.2020.140125.

[21] T. Suo, Y. Li, F. Zhao, X. Fan, W. Guo, Compressive behavior and rate-controlling mechanisms of ultrafine grained copper over wide temperature and strain rate ranges, Mech. Mater. (2013) 61, https://doi.org/10.1016/j.mechmat.2013.02.003.

[22] Q. Wei, Strain rate effects in the ultrafine grain and nanocrystalline regimes-influence on some constitutive responses, J. Mater. Sci. 42 (2007), https://doi.org/10.1007/s10853-006-0700-9.

[23] S. Nemat-Nasser, W.G. Guo, Thermomechanical response of DH-36 structural steel over a wide range of strain rates and temperatures, Mech. Mater. 35 (2003), https://doi.org/10.1016/S0167-6636(02)00323-X.

[24] H.C. Rogers, Adiabatic plastic deformation, Annu. Rev. Mater. Sci. 9 (1) (1979) 283–311, https://doi.org/10.1146/annurev.ms.09.080179.001435.

[25] V.F. Nesterenko, M.A. Meyers, J.C. LaSalvia, M.P. Bondar, Y.J. Chen, Y. L. Lukyanov, Shear localization and recrystallization in high-strain, high-strain-rate deformation of tantalum, Mater. Sci. Eng. 229 (1997), https://doi.org/10.1016/s0921-5093(96)10847-9.

[26] R.W. Chen, K.S. Vecchio, Microstructural characterization of shear band formation in Al-Li alloys, J. Phys. IV : JP 4 (1994), https://doi.org/10.1051/jp4:1994871.

[27] W.S. Lee, W.C. Sue, C.F. Lin, C.J. Wu, Strain rate and temperature dependence of the dynamic impact properties of 7075 aluminum alloy, J. Mater. Process. Technol. 100 (2000), https://doi.org/10.1016/S0924-0136(99)00465-3.

[28] U. Andrade, M.A. Meyers, K.S. Vecchio, A.H. Chokshi, Dynamic recrystallization in high-strain, high-strain-rate plastic deformation of copper, Acta Metall. Mater. 42 (1994), https://doi.org/10.1016/0956-7151(94)90417-0.

[29] A. Molinari, C. Musquar, G. Sutter, Adiabatic shear banding in high speed machining of Ti-6Al-4V: experiments and modeling, Int. J. Plast. 18 (4) (2002) 443–459.

[30] G.B. Olson, M. Cohen, Kinetics of strain-induced martensitic nucleation, Metall. Trans. A 6 (1975), https://doi.org/10.1007/BF02672301.

[31] E. Sequoia, G.B. Olson, M. Cohen, Journal of the less-common Metals A mechanism for the STRAIN-INDUCED nucleation of martensitic transformations, Journal of the Less Common Metals 18 (1) (1972), https://doi.org/10.1016/0022-5088(72)90173-7.

[32] D. Fahr, Stress- and strain-induced formation of martensite and its effects on strength and ductility of metastable austenitic stainless steels, Metall. Trans. A 2 (1971), https://doi.org/10.1007/BF02913420.

[33] J. Van Slycken, P. Verleysen, J. Degrieck, J. Bouquerel, B.C. De Cooman, Dynamic response of aluminium containing TRIP steel and its constituent phases, Mater. Sci. Eng. (2007) 460–461, https://doi.org/10.1016/j.msea.2007.01.075.

[34] M.R. Berrahmoune, S. Berveiller, K. Inal, A. Moulin, E. Patoor, Analysis of the martensitic transformation at various scales in TRIP steel, Mater. Sci. Eng. 378 (2004), https://doi.org/10.1016/j.msea.2003.10.372.

[35] S. Lee, S.J. Lee, S. Santhosh Kumar, K. Lee, B.C.D. Cooman, Localized deformation in multiphase, ultra-fine-grained 6 Pct Mn transformation-induced plasticity steel, in: Metall Mater Trans A Phys Metall Mater Sci, 2011, https://doi.org/10.1007/s11661-011-0636-9.

[36] Z. He, Y. He, Y. Ling, Q. Wu, Y. Gao, L. Li, Effect of strain rate on deformation behavior of TRIP steels, J. Mater. Process. Technol. 212 (2012), https://doi.org/10.1016/j.jmatprotec.2012.05.020.

[37] J.R. Patel, M. Cohent, Criterion for the action of applied stress in the martensitic transformation, Acta Metall. 1 (1953), https://doi.org/10.1016/0001-6160(53)90083-2.

[38] Z. Li, C.C. Tasan, K.G. Pradeep, D. Raabe, A TRIP-assisted dual-phase high-entropy alloy: grain size and phase fraction effects on deformation behavior, Acta Mater. 131 (2017) 323–335, https://doi.org/10.1016/j.actamat.2017.03.069.

[39] Z. Li, K.G. Pradeep, Y. Deng, D. Raabe, C.C. Tasan, Metastable high-entropy dual-phase alloys overcome the strength-ductility trade-off, Nature 534 (2016) 227–230, https://doi.org/10.1038/nature17981.

[40] L. Wang, C. Fu, Y. Wu, R. Li, X. Hui, Y. Wang, Superelastic effect in Ti-rich high entropy alloys via stress-induced martensitic transformation, Scripta Mater. 162 (2019), https://doi.org/10.1016/j.scriptamat.2018.10.035.

[41] H. Huang, Y. Wu, J. He, H. Wang, X. Liu, K. An, W. Wu, Z. Lu, Phase-transformation ductilization of Brittle high-entropy alloys via Metastability engineering, Adv. Mater. 29 (2017), https://doi.org/10.1002/adma.201701678.

[42] Y. Tanaka, Y. Himuro, R. Kainuma, Y. Sutou, T. Omori, K. Ishida, Ferrous polycrystalline shape-memory alloy showing huge superelasticity, Science 327 (2010), https://doi.org/10.1126/science.1183169, 1979.

[43] C. Zhang, Q. Yu, Y.T. Tang, M. Xu, H. Wang, C. Zhu, J. Ell, S. Zhao, B. E. MacDonald, P. Cao, J.M. Schoenung, K.S. Vecchio, R.C. Reed, R.O. Ritchie, E. J. Lavernia, Strong and ductile FeNiCoAl-based high-entropy alloys for cryogenic to elevated temperature multifunctional applications, Acta Mater. 242 (2023), https://doi.org/10.1016/j.actamat.2022.118449.

[44] J.M. Cabrera, J.M. Prado, M.A. Barrón, Inverse analysis of the hot uniaxial compression test by means of the finite element method, Steel Res. 70 (1999), https://doi.org/10.1002/srin.199905601.

[45] B. Voyzelle, J.D. Boyd, High-temperature deformation behaviour of Fe3Al, Mater. Sci. Eng., A 258 (1998), https://doi.org/10.1016/s0921-5093(98)00940-x.

[46] K.T. Ramesh, High Strain Rate and Impact Experiments. Part D 33, Handbook of Experimental Solid Mechanics, 2008.

[47] R. Othman, The Kolsky-Hopkinson Bar Machine, 2018, https://doi.org/10.1007/978-3-319-71919-1.

[48] H. Couque, The use of the direct impact Hopkinson pressure bar technique to describe thermally activated and viscous regimes of metallic materials, Phil. Trans. Math. Phys. Eng. Sci. (2014) 372, https://doi.org/10.1098/rsta.2013.0218.

[49] C. Zhu, T. Harrington, G.T. Gray, K.S. Vecchio, Dislocation-type evolution in quasi-statically compressed polycrystalline nickel, Acta Mater. 155 (2018), https://doi.org/10.1016/j.actamat.2018.05.022.

[50] C. Zhu, T. Harrington, V. Livescu, G.T. Gray, K.S. Vecchio, Determination of geometrically necessary dislocations in large shear strain localization in aluminum, Acta Mater. 118 (2016), https://doi.org/10.1016/j.actamat.2016.07.051.

[51] B.H. Toby, R.B. Von Dreele, GSAS-II: the genesis of a modern open-source all purpose crystallography software package, J. Appl. Crystallogr. 46 (2013), https://doi.org/10.1107/S0021889813003531.

[52] Y. Geng, D. Lee, X. Xu, M. Nagasako, M. Jin, X. Jin, T. Omori, R. Kainuma, Coherency of ordered γ′ precipitates and thermoelastic martensitic transformation in FeNiCoAlTaB alloys, J. Alloys Compd. 628 (2015) 287–292, https://doi.org/10.1016/j.jallcom.2014.12.172.

[53] L. Jian, C.C. Chou, C.M. Wayman, Martensitic transformation and the shape memory effect in an Fe-33Ni-12Co-5Ti alloy, Mater. Chem. Phys. 34 (1993), https://doi.org/10.1016/0254-0584(93)90113-Z.

[54] T. Maki, S. Furutani, I. Tamur, Shape memory effect related to thin plate martensite with large thermal hysteresis in ausaged Fe-Ni-Co-Ti alloy, ISIJ Int. 29 (1989) 438–445, https://doi.org/10.2355/isijinternational.29.438.

[55] C. Zhang, C. Zhu, S. Shin, L. Casalena, K. Vecchio, Grain boundary precipitation of tantalum and NiAl in superelastic FeNiCoAlTaB alloy, Mater. Sci. Eng. 743 (2019) 372–381, https://doi.org/10.1016/j.msea.2018.11.077.

[56] B. Bay, N. Hansen, D. Kuhlmann-Wilsdorf, Deformation structures in lightly rolled pure aluminium, Mater. Sci. Eng. 113 (1989), https://doi.org/10.1016/0921-5093(89)90325-0.

[57] D. Kuhlmann-Wilsdorf, Theory of plastic deformation: - properties of low energy dislocation structures, Mater. Sci. Eng. 113 (1989), https://doi.org/10.1016/0921-5093(89)90290-6.

[58] I. Gutierrez-Urrutia, D. Raabe, Microbanding mechanism in an Fe-Mn-C high-Mn twinning-induced plasticity steel, Scripta Mater. 69 (2013) 53–56, https://doi.org/10.1016/j.scriptamat.2013.03.010.

[59] V. Gerold, H.P. Karnthaler, ON the origin of planar slip in F.C.C. Alloys, Acta Metall. 37 (8) (1989) 2177–2183, https://doi.org/10.1016/0001-6160(89)90143-0.

[60] S. Guo, S. Sui, M. Wang, X. Hao, H. Chen, C. Wang, B. Huang, X. Lin, Overcoming strength-ductility trade-off in high-entropy alloys by tuning chemical short-range order and grain size, Intermetallics 150 (2022), https://doi.org/10.1016/j.intermet.2022.107693.

[61] Y. Wu, F. Zhang, X. Yuan, H. Huang, X. Wen, Y. Wang, M. Zhang, H. Wu, X. Liu, H. Wang, S. Jiang, Z. Lu, Short-range ordering and its effects on mechanical properties of high-entropy alloys, J. Mater. Sci. Technol. 62 (2021) 214–220, https://doi.org/10.1016/j.jmst.2020.06.018.

[62] E. Antillon, C. Woodward, S.I. Rao, B. Akdim, T.A. Parthasarathy, Chemical short range order strengthening in a model FCC high entropy alloy, Acta Mater. 190 (2020), https://doi.org/10.1016/j.actamat.2020.02.041.

[63] F. Walsh, A. Abu-Odeh, M. Asta, Reconsidering short-range order in complex concentrated alloys, MRS Bull. 48 (2023), https://doi.org/10.1557/s43577-023-00555-y.

[64] F. Walsh, M. Zhang, R.O. Ritchie, A.M. Minor, M. Asta, Extra electron reflections in concentrated alloys do not necessitate short-range order, Nat. Mater. 22 (2023) 926–929, https://doi.org/10.1038/s41563-023-01570-9.

[65] S.P. Tsai, Y.T. Tsai, Y.W. Chen, P.J. Chen, P.H. Chiu, C.Y. Chen, W.S. Lee, J. W. Yeh, J.R. Yang, High-entropy CoCrFeMnNi alloy subjected to high-strain-rate compressive deformation, Mater. Char. 147 (2019) 193–198, https://doi.org/10.1016/j.matchar.2018.10.028.

[66] R. Keller, W. Zielinski, W.W. Gerberich, On the onset of low-energy dislocation substructures in fatigue: grain size effects, Mater. Sci. Eng. 113 (1989), https://doi.org/10.1016/0921-5093(89)90315-8.

[67] A.B. Greninger, A.R. Troiano, The mechanism of Martensite formation, JOM 1 (1949), https://doi.org/10.1007/bf03398900.

[68] H. Fu, W. Li, S. Song, Y. Jiang, J. Xie, Effects of grain orientation and precipitates on the superelasticity in directionally solidified FeNiCoAlTaB shape memory alloy, J. Alloys Compd. 684 (2016) 556–563, https://doi.org/10.1016/j.jallcom.2016.05.209.

[69] G.B. Olson, M. Cohen, Interphase-boundary dislocations and the concept of coherency, Acta Metall. 27 (1979), https://doi.org/10.1016/0001-6160(79)90081-6.

[70] S. Nemat-Nasser, J.Y. Choi, W.G. Guo, J.B. Isaacs, Very high strain-rate response of a NiTi shape-memory alloy, in: Mechanics of Materials, 2005, https://doi.org/10.1016/j.mechmat.2004.03.007.

[71] C. Li, J.H. Chen, X. Wu, S. van der Zwaag, Effect of strain rate on stress-induced martensitic formation and the compressive properties of Ti-V-(Cr,Fe)-Al alloys, Mater. Sci. Eng. 573 (2013), https://doi.org/10.1016/j.msea.2013.03.002.

[72] Y. Geng, M. Jin, W. Ren, W. Zhang, X. Jin, Effects of aging treatment on martensitic transformation of Fe-Ni-Co-Al-Ta-B alloys, J. Alloys Compd. 577 (2013), https://doi.org/10.1016/j.jallcom.2012.03.033.

[73] Y. Tanaka, R. Kainuma, T. Omori, K. Ishida, Alloy design for Fe-Ni-Co-Al-based superelastic alloys, in: Mater Today Proc, 2015, https://doi.org/10.1016/j.matpr.2015.07.333.

[74] D. Lee, T. Omori, R. Kainuma, Ductility enhancement and superelasticity in Fe-Ni-Co-Al-Ti-B polycrystalline alloy, J. Alloys Compd. 617 (2014), https://doi.org/10.1016/j.jallcom.2014.07.136.

[75] ASTM E 562. Standard test method for determining volume fraction by systematic manual point count, ASTM international, 2008.

[76] J.R.C. Guimarães, The deformation-induced martensitic reaction in polycrystalline Fe - 30.7 Ni - 0.06C, Scripta Metall. 6 (1972), https://doi.org/10.1016/0036-9748(72)90049-X.

[77] J.R.C. Guimarães, J.C. Gomes, M.A. Meyers, The effects of shock loading and grain refining on the kinetics of deformation induced martensite in Fe-31% Ni-0.1%C, Transactions of the Japan Institute of Metals 18 (1977), https://doi.org/10.2320/matertrans1960.18.803.

[78] S. Morito, H. Saito, T. Ogawa, T. Furuhara, T. Maki, Effect of austenite grain size on the morphology and crystallography of lath martensite in low carbon steels, ISIJ Int. 45 (2005), https://doi.org/10.2355/isijinternational.45.91.

[79] D. Rittel, L.H. Zhang, S. Osovski, The dependence of the Taylor–Quinney coefficient on the dynamic loading mode, J. Mech. Phys. Solid. 107 (2017), https://doi.org/10.1016/j.jmps.2017.06.016.

[80] G.C. Soares, M. Patnamsetty, P. Peura, M. Hokka, Effects of adiabatic heating and strain rate on the dynamic response of a CoCrFeMnNi high-entropy alloy, Journal of Dynamic Behavior of Materials 5 (2019) 320–330, https://doi.org/10.1007/s40870-019-00215-w.

[81] M.B. Bever, D.L. Holt, A.L. Titchener, The stored energy of cold work, Prog. Mater. Sci. 17 (1973), https://doi.org/10.1016/0079-6425(73)90001-7.

[82] H.A. Padilla, C.D. Smith, J. Lambros, A.J. Beaudoin, I.M. Robertson, Effects of deformation twinning on energy dissipation in high rate deformed zirconium, in: Metall Mater Trans A Phys Metall Mater Sci, 2007, https://doi.org/10.1007/s11661-007-9365-5.

[83] M.A. Meyers, J. LaSalvia, V.F. Nesterenko, Y. Chen, B. Kad, Dynamic recrystallization in high strain rate deformation, in: T. McNelly (Ed.), Recrystallization and Related Phenomena, Monterey, 1997, pp. 279–286.

[84] N. Yan, Z. Li, Y. Xu, M.A. Meyers, Shear localization in metallic materials at high strain rates, Prog. Mater. Sci. 119 (2021), https://doi.org/10.1016/j.pmatsci.2020.100755.

[85] P.A.J. Bagot, O.B.W. Silk, J.O. Douglas, S. Pedrazzini, D.J. Crudden, T.L. Martin, M.C. Hardy, M.P. Moody, R.C. Reed, An Atom Probe Tomography study of site preference and partitioning in a nickel-based superalloy, Acta Mater. 125 (2017), https://doi.org/10.1016/j.actamat.2016.11.053.

[86] A. Evirgen, J. Ma, I. Karaman, Z.P. Luo, Y.I. Chumlyakov, Effect of aging on the superelastic response of a single crystalline FeNiCoAlTa shape memory alloy, Scripta Mater. 67 (2012), https://doi.org/10.1016/j.scriptamat.2012.06.006.

[87] Q. Wang, Z. Li, S. Pang, X. Li, C. Dong, P.K. Liaw, Coherent precipitation and strengthening in compositionally complex alloys: a review, Entropy 20 (2018), https://doi.org/10.3390/e20110878.

[88] A.J. Ardell, Precipitation hardening, Metall. Trans. A 16 (1985) 2131–2165, https://doi.org/10.1007/BF02670416.

[89] J. Ma, B.C. Hornbuckle, I. Karaman, G.B. Thompson, Z.P. Luo, Y.I. Chumlyakov, The effect of nanoprecipitates on the superelastic properties of FeNiCoAlTa shape memory alloy single crystals, Acta Mater. 61 (2013) 3445–3455, https://doi.org/10.1016/j.actamat.2013.02.036.

[90] T.M. Pollock, A.S. Argon, Creep resistance of CMSX-3 nickel base superalloy single crystals, Acta Metall. Mater. 40 (1992), https://doi.org/10.1016/0956-7151(92)90195-K.

[91] J. Douin, P. Veyssière, P. Beauchamp, Dislocation line stability in Ni_3Al, in: Philosophical Magazine A: Physics of Condensed Matter, Structure, Defects and

Mechanical Properties, vol. 54, 1986, https://doi.org/10.1080/01418618608240722.
[92] N. Hansen, Hall-petch relation and boundary strengthening, Scripta Mater. 51 (2004), https://doi.org/10.1016/j.scriptamat.2004.06.002.
[93] C. Varvenne, A. Luque, W.A. Curtin, Theory of strengthening in fcc high entropy alloys, Acta Mater. 118 (2016), https://doi.org/10.1016/j.actamat.2016.07.040.
[94] C. Varvenne, G.P.M. Leyson, M. Ghazisaeidi, W.A. Curtin, Solute strengthening in random alloys, Acta Mater. 124 (2017), https://doi.org/10.1016/j.actamat.2016.09.046.
[95] B. Liu, D. Raabe, P. Eisenlohr, F. Roters, A. Arsenlis, G. Hommes, Dislocation interactions and low-angle grain boundary strengthening, Acta Mater. 59 (2011), https://doi.org/10.1016/j.actamat.2011.07.067.
[96] D.A. Hughes, N. Hansen, Microstructure and strength of nickel at large strains, Acta Mater. 48 (2000) 2985–3004, https://doi.org/10.1016/S1359-6454(00)00082-3.
[97] W. Guo, J. Su, W. Lu, C.H. Liebscher, C. Kirchlechner, Y. Ikeda, F. Körmann, X. Liu, Y. Xue, G. Dehm, Dislocation-induced breakthrough of strength and ductility trade-off in a non-equiatomic high-entropy alloy, Acta Mater. 185 (2020) 45–54, https://doi.org/10.1016/j.actamat.2019.11.055.
[98] Z. Wang, I. Baker, Z. Cai, S. Chen, J.D. Poplawsky, W. Guo, The effect of interstitial carbon on the mechanical properties and dislocation substructure evolution in $Fe_{40.4}Ni_{11.3}Mn_{34.8}Al_{7.5}Cr_6$ high entropy alloys, Acta Mater. 120 (2016) 228–239, https://doi.org/10.1016/j.actamat.2016.08.072.
[99] C. Zhang, C. Zhu, K. Vecchio, Non-equiatomic FeNiCoAl-based high entropy alloys with multiscale heterogeneous lamella structure for strength and ductility, Mater. Sci. Eng. 743 (2019) 361–371, https://doi.org/10.1016/j.msea.2018.11.073.
[100] J.R.C. Guimarães, R.J. De Angelis, Hardening by a deformation induced phase transformation, Mater. Sci. Eng. 15 (1974), https://doi.org/10.1016/0025-5416(74)90063-9.
[101] D.C. Ludwigson, J.A. Berger, Plastic behaviour of metastable austenitic stainless steels, J. Iron Steel Inst. 207 (1969).
[102] L.F. Ramos, D.K. Matlock, G. Krauss, On the deformation behavior of dual-phase steels, Metall. Trans. A 10 (1979) 259–261, https://doi.org/10.1007/BF02817636.
[103] R.G. Davies, The deformation behavior of a vanadium-strengthened dual phase steel, Metall. Trans. A 9 (1978), https://doi.org/10.1007/BF02647169.
[104] N. Jost, Thermal fatigue of Fe-Ni-Co-Ti shape-memory-alloys, Mater. Sci. Eng. (1999) 273–275, https://doi.org/10.1016/S0921-5093(99)00341-X.